Spatiotemporal distribution of β-amyloid in Alzheimer's disease results from heterogeneous regional carrying capacities

Alex Whittington[1], David J. Sharp[1], Roger N. Gunn[1,2,3,*]; Alzheimer's Disease Neuroimaging Initiative[#]

1. Division of Brain Sciences, Imperial College London, Hammersmith Hospital Campus, London, UK
2. Imanova Ltd, London, UK
3. Department of Engineering Science, Institute of Biomedical Engineering, University of Oxford, Oxford, UK.

Corresponding author

Professor Roger N Gunn,

Division of Brain Sciences, Burlington Danes Building,

Hammersmith Hospital, Du Cane Road,

London, W12 0NN, UK.

Email: r.gunn@imperial.ac.uk.

Telephone: +44 (0)208 008 6000.

Fax: +44 (0)208 008 6491.

Word count: 4985 words

ABSTRACT

β-amyloid (Aβ) accumulation in the brain is one of two pathological hallmarks of Alzheimer's Disease (AD) and its spatial distribution has been studied extensively *ex vivo.* We apply mathematical modelling to Aβ *in vivo* Positron Emission Tomography (PET) imaging data in order to investigate competing theories of Aβ spread in AD. Our results provide evidence that Aβ accumulation starts in all brain regions simultaneously and that its spatiotemporal distribution is a result of heterogeneous regional carrying capacities (regional maximum possible concentration of Aβ) for the aggregated protein rather than longer term spreading from seed regions.

INTRODUCTION

The major constituent of neuritic plaques which appear to play a key role in the pathogenesis of AD(*1–3*) is Aβ(*4,5*). The spatiotemporal distribution of Aβ in AD has been extensively characterised *ex vivo* through neuropathological studies employing Aβ immunostaining(*6–8*). A consistent spatiotemporal distribution is observed with Aβ initially restricted to a small number of brain regions before becoming widespread later in the disease(*6,8*). There are competing hypotheses for the biological mechanism causing the evolution of Aβ pathology. One hypothesis is that, Aβ accumulation is determined by properties of the local tissue environment(*9–12*). A second hypothesis is that, Aβ originates in a small number of seed regions and over the duration of the disease spreads to other brain regions, for example by "prion-like" self-propagation or transynaptic spread(*7,13–16*).

The *in vivo* regional Aβ concentration can be measured in humans using PET. Large cohort cross-sectional studies have been performed(*17,18*) but analysis has mainly focused on classifying the distinct clinical phases of the disease. This approach has provided relatively little information about the way Aβ plaques accumulate over time. Analysis of longitudinal studies has either been restricted to short time windows of no more than 2 years(*19–21*) or to studying the average deposition across the whole cortex(*22*). Thus, despite the large amount of *in vivo* data collected, a full characterisation of the spatiotemporal distribution of Aβ has yet to be performed.

The logistic growth model has previously used to model the growth of a wide range of biological and clinical phenomena such as the spread of forest expansions postglacial expansion of forest trees[23], the *in vitro* pharmacodynamics of bactericidal kinetics[24] and most interestingly *in vitro* Aβ fibrillation[25]. Here, the logistic growth model is introduced to provide a mathematical description of a sigmoidal increase in $A\beta$ concentration over time (see Fig. 1),

$$
\begin{aligned}
SUVr(t) &= NS + A\beta(t) \\
&= NS + \frac{K}{1+e^{-r(t-T_{50})}}
\end{aligned}
\tag{1}
$$

where t is the time through the accumulation process (t=0 corresponds to a time point where Aβ levels are minimal), $SUVr(t)$ is the PET $A\beta$ standardised uptake value ratio, $A\beta(t)$ is the concentration of Aβ at time t, NS is the tracer non-specific binding, r is the exponential uninhibited growth rate, T_{50} is the time of half maximal $A\beta$ concentration and K is the carrying capacity.

It is possible to test between the two competing hypotheses of Aβ accumulation by considering whether each of the four model parameters is constant across different brain regions or whether they are regionally different. A summary of the different logistic growth models is displayed in Fig. 2. If the T_{50} varies between regions then the model is consistent with longer term spreading from seed regions as seed regions would have a lower T_{50} than other regions (models shown in grey in Fig. 2). If T_{50} is constant across the brain it is consistent with local tissue properties driving the accumulation process (models shown in white in Fig. 2). Application of statistical model selection criteria allows us to test between the competing hypotheses.

We take this novel approach to test between the competing models of Aβ accumulation.
We use the whole cortex Aβ profile derived from the longitudinal study (where the
patients did not receive any treatment) of Jack et al.(*26*) to transform a large cross-
sectional study into a chronological data set by assigning each subject in the cross-
sectional dataset a time through the accumulation process. This dataset enables full
spatiotemporal modelling of the Aβ accumulation process in AD, at a population level.
Applying the logistic growth model to *in vivo* Aβ accumulation in this dataset allows us
to test whether accumulation is best explained by the longer term spreading of amyloid
from seed regions or by heterogeneous regional carrying capacities across brain regions.

MATERIALS AND METHODS

Longitudinal model of Aβ accumulation

A logistic growth model is introduced for the description of accumulation of Aβ

concentration in the human brain. The model assumes that the growth rate of Aβ

concentration is proportional to the product of the current concentration of Aβ and a term

limiting growth due to the carrying capacity of the local environment. The model is

defined by the following differential equation,

$$\frac{dA\beta(t)}{dt} = rA\beta(t)\left(1 - \frac{K}{A\beta(t)}\right) \tag{4}$$

where $A\beta(t)$ is the concentration of Aβ at time t, r is the uninhibited exponential

growth rate and K is the carrying capacity. Solving the differential equation yields a

function for the concentration of Aβ over time,

$$A\beta(t) = \frac{K}{1 + e^{-r(t - T_{50})}} \tag{5}$$

where T_{50} is the time of half maximal $A\beta$ concentration (i.e. $A\beta(T_{50}) = \frac{K}{2}$).

In vivo PET amyloid tracers are quantified in terms of the SUVr between a target region

containing amyloid and a reference region containing only background non-specific

binding and therefore,

$$SUVr(t) = NS + A\beta(t) \tag{6}$$

where NS is the non-specific binding component of the imaging outcome measure SUVr.

Combining equations 2 and 3 yields equation 1 that describes the temporal evolution of the *in vivo* PET β-amyloid signal over time (with the 4 parameters NS, r, T_{50} and K),

Imaging data

A chronological Aβ dataset for the AD disease pathway at the population level was generated by transforming a large cross-sectional Aβ dataset using a population time course for the mean cortical SUVr obtained in a smaller longitudinal study.

Cross-sectional ^{18}F-AV45 human $A\beta$ PET imaging data and structural Magnetic Resonance Imaging (MRI) data were obtained from the Alzheimer's Disease Neuroimaging Initiative (ADNI) database(*27*) for 779 subjects. The ADNI was launched in 2003 as a public-private partnership, led by Principal Investigator Michael W. Weiner, MD. The primary goal of ADNI has been to test whether serial MRI, PET, other biological markers, and clinical and neuropsychological assessment can be combined to measure the progression of mild cognitive impairment and early Alzheimer's disease. For up-to-date information, see www.adni-info.org.

^{18}*F-AV45 HUMAN* $A\beta$ *PET IMAGING DATA.* Each subject underwent a 20-minute ^{18}F-AV45 PET scan 50 minutes post-injection (370±37 MBq) according to the standardised ADNI protocol(*28*). There were 3 image pre-processing steps applied to the data prior to entry into the ADNI imaging database (For full details, see http://adni.loni.usc.edu/methods/pet-analysis/pre-processing). Briefly, 4 late-time 5 minute frames are co-registered and averaged. The resulting image is converted to a 160x160x96 voxel static image with voxel dimension of 1.5mmx1.5mmx1.5mm.

Finally, an 8mm full width half maximum gaussian filter was applied (corresponding to the lowest resolution scanner used in the study). These primary data were downloaded from the ADNI database and used in the subsequent analyses.

T1-WEIGHTED MRI DATA. All subjects underwent T1-weighted 1.5T structural MRI which were downloaded from the ADNI imaging database.

Image Processing

REGISTRATION OF IMAGES INTO STEREOTACTIC SPACE. ^{18}F-AV45 data were nonlinearly registered into Montreal Neurological Institute 152 space (MNI152 space[29]) using DARTEL[30]. Initially the structural MRI images were segmented into grey matter and white matter using SPM12 and registered to a group average template. The group average template was then registered to MNI152 space. Each subjects' ^{18}F-AV45 SUVr image was registered to the corresponding MRI using a rigid-body registration. Finally, the individuals' DARTEL flow field and template transformation was applied without modulation resulting in ^{18}F-AV45 images in MNI152 space. The normalised maps were spatially smoothed (8mm full width at half maximum Gaussian kernel). Each registration was visually assessed with 10 subjects data being rejected. Therefore, the final data set used to construct the chronological data contained 769 subjects.

CALCULATION OF SUVR DATA. A neuroanatomical atlas (CIC atlas[31]) containing 90 cortical and subcortical regions and a grey matter probability atlas in MNI

space were employed to calculate SUVr data. SUVr data were quantified using the grey matter cerebellum as the reference region which was defined as the intersection between the cerebellum region of interest (ROI) of the CIC atlas and the grey matter atlas with p(grey matter) > 0.5. The mean uptake value for the grey matter cerebellum ROI was obtained and each image was divided by this to generate an SUVr image for each subject. Finally, the 90 ROIs were applied to this image in order to derive regional SUVr values for each subject. Finally, an average cortical SUVr value was obtained by calculating the mean SUVr value for all 76 cortical regions (weighted by region volume).

Construction of Population level chronological Aβ data

Jack et al.([26]) have previously presented a functional form describing the time course of mean cortical SUVr in AD by integrating rates of change of SUVr in a longitudinal study. Demographics for the study are summarised in Table 1.

CONVERSION OF FUNCTIONAL FORM INTO ^{18}F-AV45 SUVR UNITS. The functional form([26]) (kindly provided to us by Jack) was derived from a longitudinal Aβ imaging data using ^{11}C-PiB rather than ^{18}F-AV45. Previous work scanning the same subjects with both ^{11}C-PiB and ^{18}F-AV45 has shown that a linear equation can appropriately convert between the different PET tracers([32–34]) according to AV45_SUVr = a PiB_SUVr + b. Therefore, a transformation of the ^{11}C-PiB derived functional form into ^{18}F-AV45 SUVr units was performed so that the resultant function ($_{AV45}^{Ctx}SUV_r(t)$) ranged between the mean of the 2.5[th] and 97.5[th] cortical ^{18}F-AV45 SUVr

percentiles for the cross-sectional ADNI dataset (a = 0.72 and b = 0.02). $_{AV45}^{Ctx}SUV_r(t)$ describes the time course of ^{18}F-AV45 mean cortical SUVr in AD.

TIMEPOINT IN CHRONOLOGY OF AD. We used $_{AV45}^{Ctx}SUV_r(t)$ to determine a time in the chronology of AD, t, for each of the 769 subjects in the cross-sectional study by calculating their mean cortical SUVr and then finding the value for t from $_{AV45}^{Ctx}SUV_r(t)$ which that SUVr corresponded to in the range 0 to 30 years. This generated a chronological data set at the population level for the spatiotemporal accumulation of Aβ with data at 769 time points over the 30-year disease cascade.

The calculated times were normally distributed with a mean of 11.8 years and a standard deviation of 5.12 years. It was verified that there was no relationship between the calculated t and SUV in the cerebellum. The test-retest variability of mean cortical ^{18}F-AV45 SUVr values has been calculated to be less than 3%(*35*). This would translate to a variability of 0.68 years in calculated time through the disease process for the median SUVr value of 1.3.

The coherence of the regional curves in the cross-sectional dataset (Fig. 3) shows that there is not only a stereotypical temporal accumulation at a global level but also that relative to that, each region has an accumulation curve which is consistent across subjects.

Regional Analysis of Aβ accumulation

The logistic growth model of Aβ accumulation (equation 1) was then fitted to the chronological data. In order to determine whether each of the 4 model parameters were constant across the whole brain or varied by region, sixteen different models were investigated corresponding to all the permutations of using either "global" (the parameter is constant across all brain regions) or "local" (the parameter varies by region) parameter values for each of the four model parameters. The full set of models are summarised in Table 2 and contain between 4 and 360 parameters.

Each of the models was fitted using a nonlinear trust-region reflective algorithm implemented in MATLAB (The Mathworks Inc, Natwick, CA) that minimised the residual sum of squared errors subject to $A\beta(0) < 0.1$ (this constraint did not occur for the optimum model). Model selection was performed using the Bayesian information criterion (BIC)(*36*) to select the most parsimonious model and a posterior probability of each model being optimum was ascertained from the weights of each model(*37–40*).

Parametric Image Analysis of Aβ accumulation

Having identified Model 11 (Global r & T_{50} and Local NS & K) as the optimal model based on the regional analysis (see Results), this model was then fitted at the voxel level to generate parametric images for NS and K. Parameter values for r and T_{50} were fixed from the regional analyses and individual voxel time course were fitted using a linearization of the model (see supplementary material).

RESULTS

Chronological Aβ dataset

A chronological Aβ ^{18}F-AV45 data set was created in stereotactic space from 769 subjects that ranged from healthy to AD. The chronological data exhibited coherent but different trajectories within individual regions providing evidence of a stereotypical spatiotemporal distribution at the population level (see Fig. 3).

Model selection and implications

Each of the logistic growth models was fitted to the chronological *in vivo* PET data at a regional level to investigate the spatiotemporal evolution of the $A\beta$ signal in the AD process. The 16 logistic growth models were successfully fitted and Model 11 was identified as the most parsimonious description of the data as determined by the BIC model selection criteria (see Table 1). The difference in BIC between Model 11 and all the other models (ΔBIC_i) is at least 267. Evidence is considered strong when ΔBIC is greater than ten[41]. The posterior probability that Model 11 is the best choice is also high (p>0.999999). The model accurately describes the time course of Aβ accumulation in all regions (see Supplemental Figs. 1 and 2). A selection of 9 regions with different levels of Aβ accumulation are displayed in Fig. 3, demonstrating the ability of the model to accurately describe distinct regional time courses.

Model 11 requires that regional values for K and tracer NS vary. In contrast, T_{50} and the r are constant across brain regions in this model. This suggests that regional variability in Aβ carrying capacities determine the distribution of Aβ concentration as regions with

higher carrying capacities will accumulate more amyloid over time. These results support the hypothesis that Aβ accumulation is limited by properties of the local tissue environment. The observation that the data is best explained by a model with a global T_{50} provides evidence against the spreading hypothesis, as long-term spreading from seed regions would imply shorter T_{50} for seed regions and therefore require models with a local T_{50} such as Model 12.

The analysis process was also run on two additional sets of ROIs; a set of 9 ROIs which are larger regions and cover the whole brain and a parcellation that is restricted to cortical regions. Model 11 was the optimum model for both these alternative analyses (see Supplemental Tables 2 and 3).

For Model 11, the highest carrying capacities were obtained in the anterior cingulate gyrus, precuneus and frontal operculum cortex (1.55, 1.50 and 1.46 SUVr units respectively), intermediate values were obtained in parts of the frontal cortex and the insular cortex (1.13 and 1.19) and lower values thalamus and the brain stem (0.48 and 0.38). The global T_{50} was 14.9 years and the global r was 0.20 yrs^{-1}.

Parametric imaging of Carrying Capacity

The regional variation normally seen in AD is predicted when Model 11 was fitted at the voxel level using the fixed global values of r (= 0.20 yrs^{-1}) and T_{50}(= 14.9 yrs) estimated from the regional analysis. Parametric images for K and NS were generated (Fig. 4.).

DISCUSSION

We have mathematically modelled the spatiotemporal distribution of amyloid in the brain as AD pathology increases with a high degree of accuracy using a logistic growth model. Our results support the hypothesis that the regional accumulation of Aβ originates at the same time with the same growth rate for all regions. The implication is that the heterogeneous Aβ distribution observed in AD is caused by a property of the local tissue environment, rather than longer term spreading from seed regions, as this would require different growth rates or times to half maximal Aβ concentration (e.g. for long term spreading T_{50} would be expected to be earlier in seed regions). If the T_{50} in different regions was found to be different, it would have been impossible to distinguish whether the time of onset for accumulation was different for different regions or whether they accumulate at different rates, however for both mechanisms a heterogeneous T_{50} across regions would be required. As this was not found, it implies that accumulation begins at the same time and occurs at the same rate across all regions.

Our analysis shows that the spatiotemporal distribution of Aβ at the population level can be accurately modelled using a 4-parameter logistic growth model, where the carrying capacity and non-specific binding vary across the brain but the growth rate and time of half maximal concentration are constant. A model with these characteristics was clearly identified as the most parsimonious model using the BIC model selection criteria. Interestingly, this model has previously been shown to be able to characterize the accumulation of Aβ in vitro(*25*).

14

There are some limitations of the current work that should be considered. Firstly, in order to model the accumulation of in AD of Aβ at the population level we have assumed that there is a consistent spatiotemporal distribution for all subjects within the cross sectional ADNI cohort, which may be an over-simplification. However, the clear coherence of individual trajectories in all brain regions (see Supplemental Figs. 1 and 2) and previous post-mortem data(*6*) provides confidence that this assumption is reasonable. Secondly, when creating the cross-sectional dataset, we have assumed that the subjects in the longitudinal data and the cross-sectional study are all following the same accumulation trajectory. Table 1 shows demographics for both the studies. Both studies have scans from healthy controls, mild cognitive impairment and AD patients and the subjects are well matched on all the characteristics apart from the number of cognitively impaired subjects which is less in the longitudinal study. Thirdly, the outcome measure that we have considered (SUVr) does not account for brain atrophy during the 30-year period and the impact this may have on Aβ signal. Studies have shown that the rate of atrophy is greatest in medial temporal regions where the rate is 0.6% per year (std = 0.7) for HC increasing to 1.5% per year (std = 0.7) in AD(*42*). With these atrophy rates, it is unlikely that atrophy would have a significant impact on the model identification and conclusions presented. Further, it has been shown that atrophy occurs after Aβ accumulates(*43*) in AD and therefore atrophy is likely not to affect out result in this analysis. In future, it will be important to further investigate the temporal relationship between regional Aβ accumulation and atrophy.

The spatiotemporal modelling of longitudinal data with the logistic growth model that has been introduced here could have much wider utility. It will be important to investigate the trajectory of Aβ accumulation in other dementias and neurodegenerative diseases where different patterns of Aβ are observed to ascertain whether the temporal process is the same but the topography is simply driven by different regional carry capacities or whether the accumulation process is actually different.

CONCLUSION

In conclusion, the *in vivo* spatiotemporal distribution of Aβ in AD can be mathematically modelled using a logistic growth model where the Aβ carrying capacity is heterogeneous across the brain but the exponential growth rate and time of half maximal Aβ concentration are constant. This suggests that the heterogeneous Aβ accumulation in AD results from different regional carrying capacities, rather than longer term spreading from a small number of seed regions.

ACKNOWLEDGEMENTS

Disclosures

Roger Gunn is a consultant for Abbvie and Cerveau.

REFERENCES

1.   Hardy JA, Higgins GA. Alzheimer's disease: the amyloid cascade hypothesis. *Sci* . 1992;256:184-185.

2.   Hardy J, Allsop D. Amyloid deposition as the central event in the aetiology of Alzheimer's disease. *Trends Pharmacol Sci*. 1991;12:383-388.

3.   Stefani M, Dobson C. Protein aggregation and aggregate toxicity: new insights into protein folding, misfolding diseases and biological evolution. *J Mol Med*. 2003;81:678-699.

4.   Glenner GG, Wong CW. Alzheimer's disease: Initial report of the purification and characterization of a novel cerebrovascular amyloid protein. *Biochem Biophys Res Commun*. 1984;120:885-890.

5.   Wong CW, Quaranta V, Glenner GG. Neuritic plaques and cerebrovascular amyloid in Alzheimer disease are antigenically related. *Proc Natl Acad Sci U S A*. 1985;82:8729-8732.

6.   Braak H, Braak E. Neuropathological stageing of Alzheimer-related changes. *Acta Neuropathol*. 1991;82:239-259.

7.   Thal DR, Rüb U, Orantes M, Braak H. Phases of Aβ-deposition in the human brain and its relevance for the development of AD. *Neurology*. 2002;58:1791-1800.

8.   Arnold SE, Hyman BT, Flory J, Damasio AR, Van Hoesen GW. The topographical and neuroanatomical distribution of neurofibrillary tangles and neuritic plaques in the cerebral cortex of patients with Alzheimer's disease. *Cereb Cortex*. 1991;1:103-116.

9.   Buckner RL, Snyder AZ, Shannon BJ, et al. Molecular, structural, and functional characterization of Alzheimer's disease: evidence for a relationship between default activity, amyloid, and memory. *J Neurosci*. 2005;25:7709-7717.

10.   Hafkemeijer A, van der Grond J, Rombouts SARB. Imaging the default mode network in aging and dementia. *Biochim Biophys Acta - Mol Basis Dis*. 2012;1822:431-441.

11.   Braga RM, Sharp DJ, Leeson C, Wise RJS, Leech R. Echoes of the brain within default mode, association, and heteromodal cortices. *J Neurosci*. 2013;33:14031-14039.

12.   Buckner RL, Andrews-Hanna JR, Schacter DL. The brain's default network: Anatomy, function, and relevance to disease. *Ann N Y Acad Sci*. 2008;1124:1-38.

13.   Song HL, Shim S, Kim DH, et al. β-Amyloid is transmitted via neuronal connections along axonal membranes. *Ann Neurol*. 2014;75:88-97.

14.   Thal DR, Capetillo-Zarate E, Del Tredici K, Braak H. The development of Amyloid beta protein deposits in the aged brain. *Sci Aging Knowl Environ*. 2006;2006:re1.

15.   Nath S, Agholme L, Kurudenkandy FR, Granseth B, Marcusson J, Hallbeck M. Spreading of neurodegenerative pathology via neuron-to-neuron transmission of β-

Amyloid. *J Neurosci*. 2012;32:8767-8777.

16. Hallbeck M, Nath S, Marcusson J. Neuron-to-neuron transmission of neurodegenerative pathology. *Neuroscientist*. 2013;19:560-566.

17. Rowe CC, Ellis KA, Rimajova M, et al. Amyloid imaging results from the Australian imaging, biomarkers and lifestyle (AIBL) study of aging. *Neurobiol Aging*. 2010;31:1275-1283.

18. Mueller SG, Weiner MW, Thal LJ, et al. Ways toward an early diagnosis in Alzheimer's disease: The Alzheimer's disease neuroimaging initiative (ADNI). *Alzheimer's Dement*. 2005;1:55-66.

19. Resnick SM, Sojkova J, Zhou Y, et al. Longitudinal cognitive decline is associated with fibrillar amyloid-beta measured by [11C]PiB. *Neurology*. 2010;74:807-815.

20. Landau SM, Fero A, Baker SL, et al. Measurement of longitudinal β-Amyloid change with 18F-Florbetapir PET and standardized uptake value ratios. *J Nucl Med*. 2015;56:567-574.

21. Villain N, Chételat G, Grassiot B, et al. Regional dynamics of amyloid-β deposition in healthy elderly, mild cognitive impairment and Alzheimer's disease: A voxelwise PiB-PET longitudinal study. *Brain*. 2012;135:2126-2139.

22. Bateman RJ, Xiong C, Benzinger TL, et al. Clinical and biomarker changes in dominantly inherited Alzheimer's disease. *N Engl J Med*. 2012;367:795-804.

23. Bennett KD. Postglacial population expansion of forest trees in Norfolk, UK. *Nature*. 1983;303:164-167.

24. Yano Y, Oguma T, Nagata H, Sasaki S. Application of logistic growth model to pharmacodynamic analysis of in vitro bactericidal kinetics. *J Pharm Sci*. 1998;87:1177-1183.

25. Lee C-C, Nayak A, Sethuraman A, Belfort G, McRae GJ. A three-stage Kinetic model of Amyloid fibrillation. *Biophys J*. 2007;92:3448-3458.

26. Jack CRJ, Wiste HJ, Lesnick TG, et al. Brain β-amyloid load approaches a plateau. *Neurology*. 2013;80:890-896.

27. Jagust WJ, Bandy D, Chen K, et al. The Alzheimer's disease neuroimaging initiative positron emission tomography core. *Alzheimer's Dement*. 2010;6:221-229.

28. Jagust WJ, Landau SM, Koeppe RA, et al. The Alzheimer's disease neuroimaging initiative 2 PET core: 2015. *Alzheimer's Dement J Alzheimer's Assoc*. 2016;11:757-771.

29. Mazziotta J, Toga A, Evans A, et al. A probabilistic atlas and reference system for the human brain: international consortium for brain mapping (ICBM). *Philos Trans R Soc London Ser B*. 2001;356:1293-1322.

30. Ashburner J. A fast diffeomorphic image registration algorithm. *Neuroimage*. 2007;38:95-113.

31. Tziortzi AC, Searle GE, Tzimopoulou S, et al. Imaging dopamine receptors in humans with [11C]-(+)-PHNO: dissection of D3 signal and anatomy. *Neuroimage*.

2011;54:264-277.

32. Landau SM, Breault C, Joshi AD, et al. Amyloid-β imaging with Pittsburgh compound B and Florbetapir: comparing radiotracers and quantification methods. *J Nucl Med*. 2013;54:70-77.

33. Landau SM, Thomas BA, Thurfjell L, et al. Amyloid PET imaging in Alzheimer's disease: a comparison of three radiotracers. *Eur J Nucl Med Mol Imaging*. 2014;41:1398-1407.

34. Wolk DA, Zhang Z, Boudhar S, Clark CM, Pontecorvo MJ, Arnold SE. Amyloid imaging in Alzheimer's disease: comparison of florbetapir and Pittsburgh compound-B positron emission tomography. *J Neurol Neurosurg Psychiatry*. 2012;83:923-926.

35. Joshi AD, Pontecorvo MJ, Clark CM, et al. Performance characteristics of amyloid PET with Florbetapir F 18 in patients with Alzheimer's disease and cognitively normal subjects. *J Nucl Med*. 2012;53:378-384.

36. Schwarz G. Estimating the dimension of a model. *Ann Stat*. 1978;6:461-464.

37. Akaike H. A Bayesian analysis of the minimum AIC procedure. *Ann Inst Stat Math*. 1978;30:9-14.

38. Akaike H. A Bayesian extension of the minimum AIC procedure of autoregressive model fitting. *Biometrika*. 1979;66:237-242.

39. Bozdogan H. Model selection and Akaike's information criterion (AIC): the general theory and its analytical extensions. *Psychometrika*. 1987;52:345-370.

40. Burnham KP, Anderson DR. Multimodel inference: understanding AIC and BIC in model selection. *Sociol Methods Res*. 2004;33:261-304.

41. Kass RE, Raftery AE. Bayes factors. *J Am Stat Assoc*. 1995;90:773-795.

42. Sluimer JD, Flier WM, Karas GB, et al. Accelerating regional atrophy rates in the progression from normal aging to Alzheimer's disease. *Eur Radiol*. 2009;19:2826-2833.

43. Jack Jr CR, Knopman DS, Jagust WJ, et al. Tracking pathophysiological processes in Alzheimer's disease: an updated hypothetical model of dynamic biomarkers. *Lancet Neurol*. 2013;12:207-216.
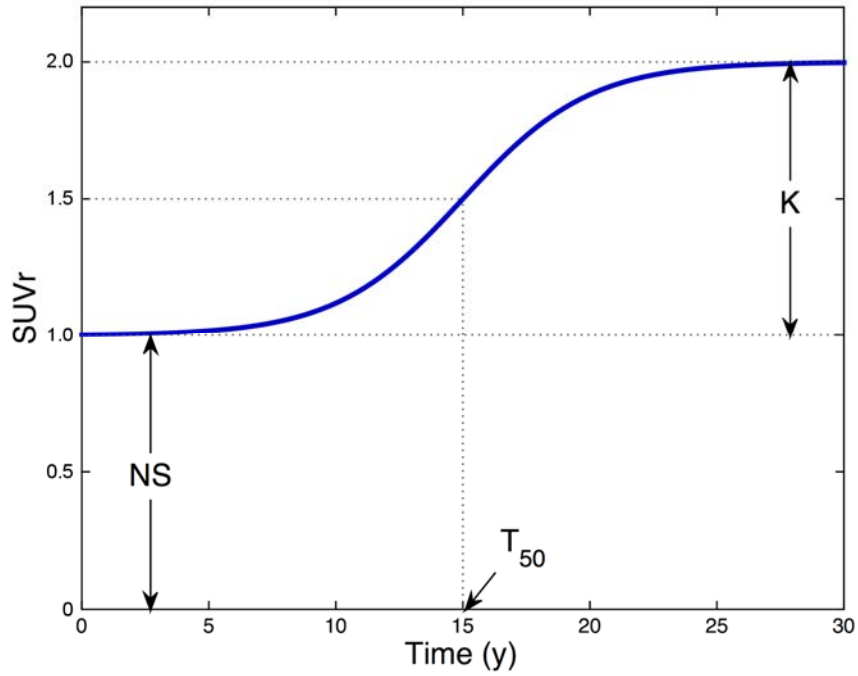
Figure 1: The logistic growth model describing the $A\beta$ PET imaging signal over time as a function of the PET tracer's non-specific binding (NS), the carrying capacity (K), the time of half maximal Aβ concentration (T_{50}) and the uninhibited exponential growth rate (r).
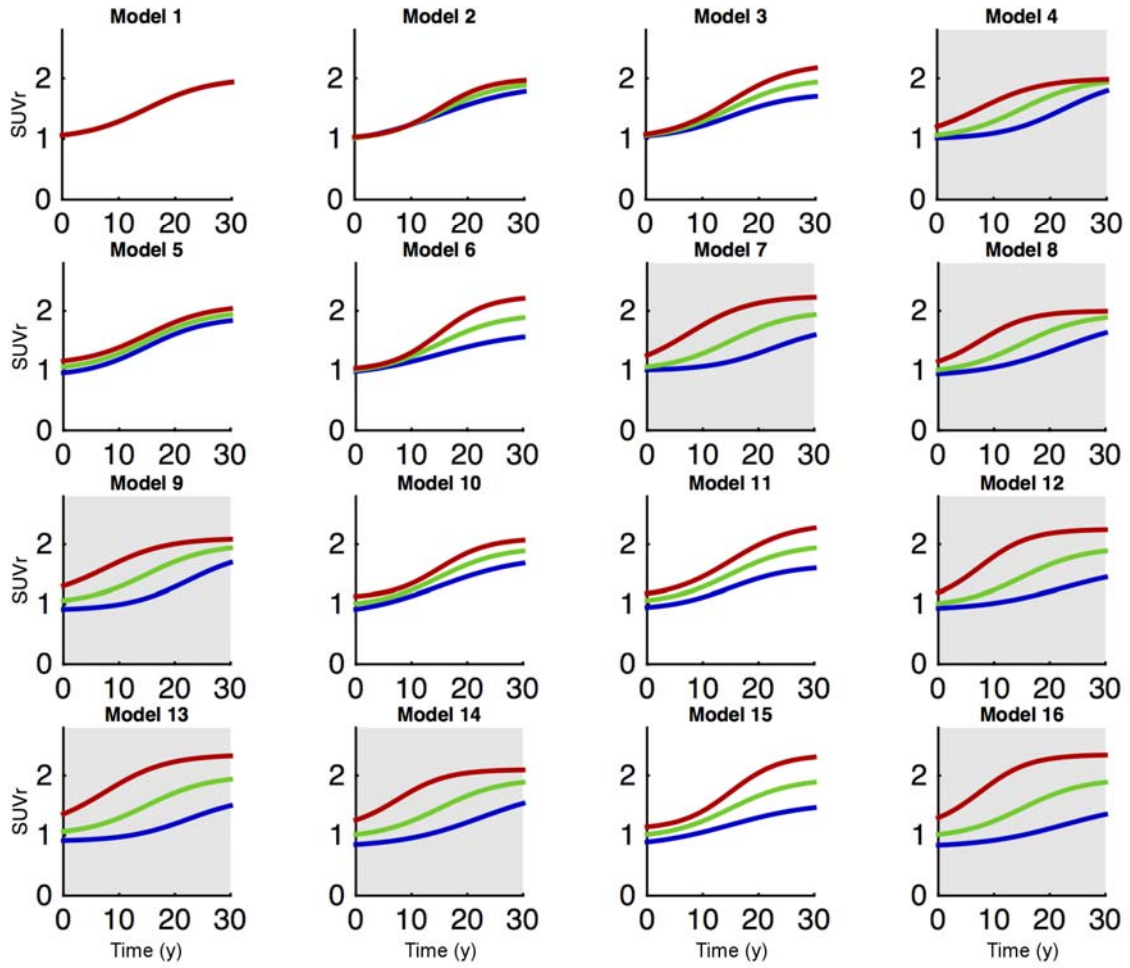
Figure 2: 16 logistic growth models of Aβ accumulation with example curves from 3 distinct brain regions. Models in grey have regionally different T_{50} values and are consistent with spreading from seed regions whist the models in white are consistent with local tissue properties driving the Aβ accumulation process.
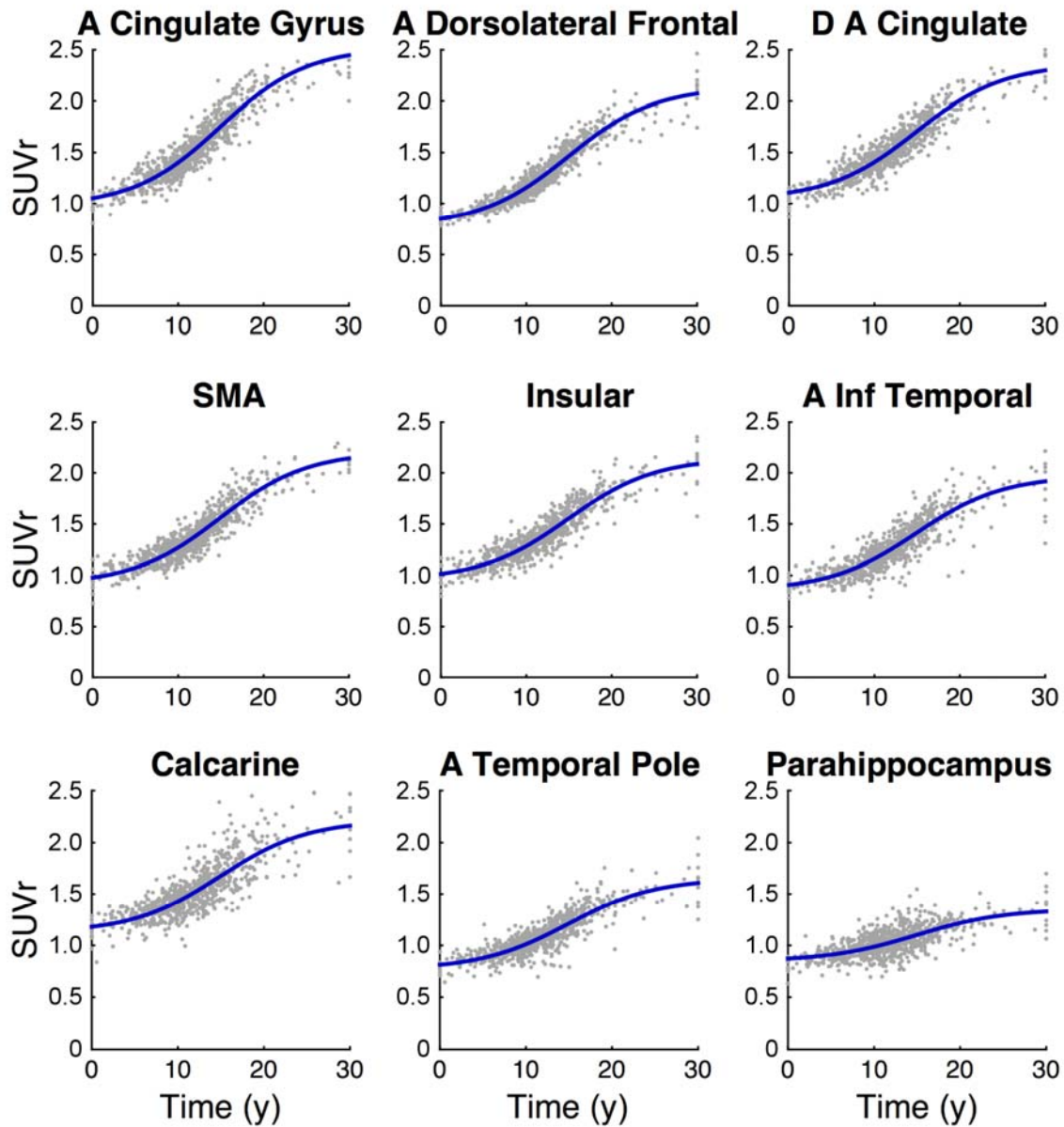
Figure 3: Model fitting of the most parsimonious logistic growth model (Model 11) to the chronological ^{18}F-AV45 Aβ PET data in 9 regions (D: Dorsal, A: Anterior, Inf: Inferior). The model accurately describes the data for regions of high (top row), medium (middle row) and low (bottom row) accumulation.
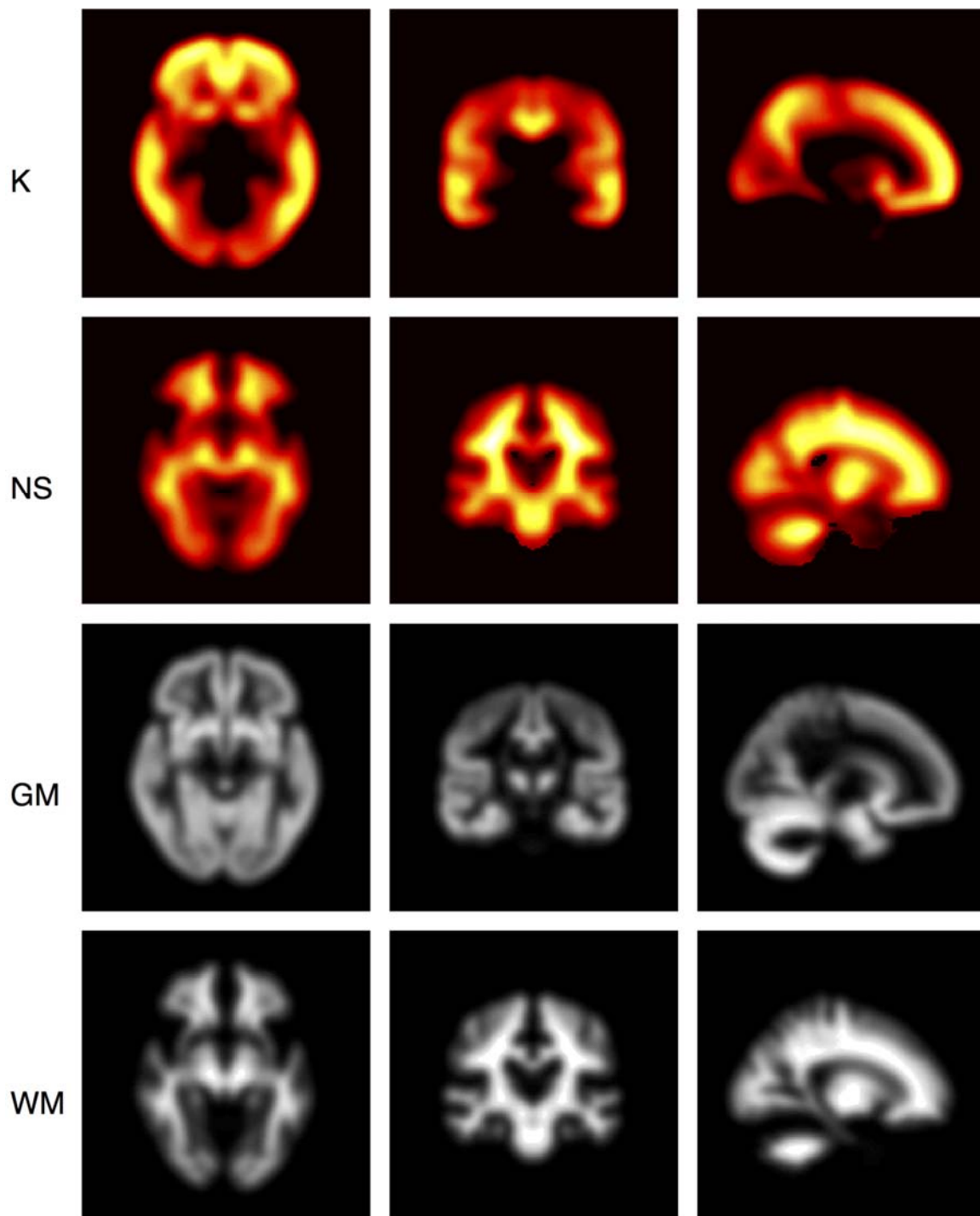
Figure 4: Parametric images displayed as orthographic projections for the carrying capacity K and the tracer non-specific binding (NS) obtained from fitting Model 11 at the voxel level. Grey matter (GM) and white matter (WM) maps are displayed for reference.

The highest carrying capacities are found in the frontal lobe and the lowest are observed in the cerebellum, occipital lobe and the brain stem. The non-specific image is consistent with the known non-specific binding of ^{18}F-AV45 to white matter.

Characteristic	Jack et al	ADNI
Number	260	769
Age – median (min max)	79 (70 94)	73 (55 91)
Male – n (%)	162 (62)	438 (57)
Number of MCI/AD patients – n (%)	55 (21)	558 (73)
APOE e4 positive – n (%)	87 (33)	342 (44)
MMSE – median (min max)	28 (23 30)	28 (19 30)

Table 1: The characteristics subjects taken from both the longitudinal study performed by Jack et al. and the cross-sectional data obtained from ADNI. These two datasets are combined to create a cross-sectional dataset.

Model	K SUVr	r yrs⁻¹	T₅₀ yrs	NS	Parameters	SSQ	ΔBICᵢ (BICᵢ - BICₘᵢₙ)
Model 1	Global	Global	Global	Global	4	3073.7	81500
Model 2	Global	Local	Global	Global	93	2273.7	61600
Model 3	Local	Global	Global	Global	93	1324.0	24200
Model 4	Global	Global	Local	Global	93	1245.7	19900
Model 5	Global	Global	Global	Local	93	1147.2	14200
Model 6	Local	Local	Global	Global	182	1131.4	14300
Model 7	Local	Global	Local	Global	182	1079.3	11000
Model 8	Global	Local	Local	Global	182	1070.2	10400
Model 9	Global	Global	Local	Local	182	1002.6	5910
Model 10	Global	Local	Global	Local	182	977.0	4120
Model 11	Local	Global	Global	Local	182	920.6	0
Model 12	Local	Local	Local	Global	271	1046.9	9890
Model 13	Local	Global	Local	Local	271	918.9	865
Model 14	Global	Local	Local	Local	271	918.8	861
Model 15	Local	Local	Global	Local	271	911.0	267
Model 16	Local	Local	Local	Local	360	908.7	1090

Table 2: The 16 parameterisations of the logistic growth model of Aβ accumulation used to analyse the chronological ^{18}F-AV45 SUVr PET data at a regional level with the corresponding sum of squared residuals (SSQ) and ΔBIC. 90 cortical and subcortical regions were included and parameters were either restricted to a single value across all regions (Global) or fitted individually for each region (Local). ΔBIC gives a measure of the parsimony of each model in relation to the smallest BIC value. Model 11 (Local K, Global r, Global T_{50} and Local NS) gives the most parsimonious fit to the data.

SUPPLEMENTARY MATERIAL

Anatomical Region Definitions

| Region #	Region Name	Region #	Region Name	Region #	Region Name
1	Insular_ctx_L	41	Inf_Temp_G_post_R	81	Cerebellum
2	Ant_Dorsolateral_Frontal_ctx_L	42	Postcentral_G_R	82	Brain Stem
3	Precentral_G_L	43	Parietal_Lobule_R	83	Anterior_Medial_Frontal_ctx_R
4	Anterior_Temp_Pole_L	44	Supramarginal_G_R	84	Poster_Medial_Frontal_ctx_R
5	Sup_Temp_G_ant_L	45	Angular_G_R	85	Anterior_Medial_Frontal_ctx_L
6	Sup_Temp_G_post_L	46	Occipital_Pole_R	86	Poster_Medial_Frontal_ctx_L
7	Middle_Temp_G_ant_L	47	Calcarine_ctx_R	87	Post_Dorsolateral_Frontal_ctx_L
8	Middle_Temp_G_post_L	48	Medial_Orbital_ctx_R	88	Post_Dorsolateral_Frontal_ctx_R
9	Inf_Temp_G_ant_L	49	SMA_R	89	Putamen_R
10	Inf_Temp_G_post_L	50	Precuneous_ctx_R	90	Putamen_L
11	Postcentral_G_L	51	Cuneus_R		
12	Parietal_Lobule_L	52	Lat_Orbital_ctx_R		
13	Supramarginal_G_L	53	Parahip_Ambiens_G_ant_R		
14	Angular_G_L	54	Parahip_Subiculum_G_post_R		
15	Occipital_Pole_L	55	Lingual_G_R		
16	Calcarine_ctx_L	56	Temp_Fusiform_ctx_ant_R		
17	Medial_Orbital_ctx_L	57	Temp_Fusiform_ctx_post_R		
18	SMA_L	58	Temp_Occip_Fusiform_ctx_R		
19	Precuneous_ctx_L	59	Occipital_Fusiform_G_R		
20	Cuneus_L	60	Frontal_Operculum_ctx_R		
21	Lat_Orbital_ctx_L	61	Central_Operculum_ctx_R		
22	Parahip_Ambiens_G_ant_L	62	Parietal_Operculum_ctx_R		
23	Parahip_Subiculum_G_post_L	63	Ventral_Cing_Subcallosal_G		
24	Lingual_G_L	64	Anterior_Cingulate_G		
25	Temp_Fusiform_ctx_ant_L	65	Posterior_Cingulate_G		
26	Temp_Fusiform_ctx_post_L	66	Dorsal_Anterior_Cingulate		
27	Temp_Occip_Fusiform_ctx_L	67	Cerebral_White_Matter_L		
28	Occipital_Fusiform_G_L	68	Caudate_L		
29	Frontal_Operculum_ctx_L	69	Globus_Pallidus_L		
30	Central_Operculum_ctx_L	70	Hippocampus_L		
31	Parietal_Operculum_ctx_L	71	Amygdala_L		
32	Insular_ctx_R	72	Accumbens_L		
33	Ant_Dorsolateral_Frontal_ctx_R	73	Cerebral_White_Matter_R		
34	Precentral_G_R	74	Caudate_R		
35	Anterior_Temp_Pole_R	75	Globus_Pallidus_R		
36	Sup_Temp_G_ant_R	76	Hippocampus_R		
37	Sup_Temp_G_post_R	77	Globus_Pallidus_R		
38	Middle_Temp_G_ant_R	78	Hippocampus_R		

| 39 | Middle_Temp_G_post_R | 79 | Thalamus_L | |
| 40 | Inf_Temp_G_ant_R | 80 | Thalamus_R | |
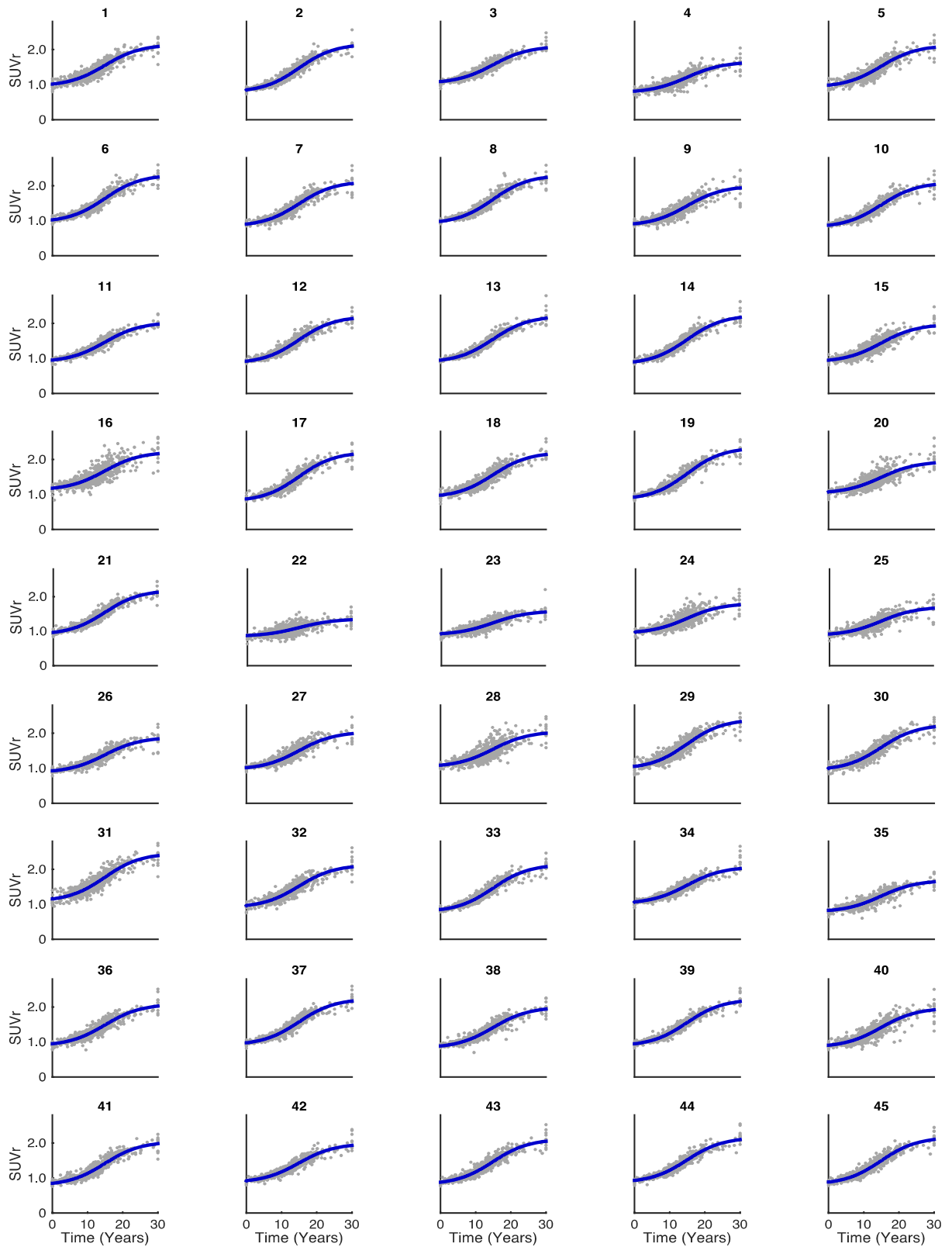
Figure S-1: Fit of the most parsimonious logistic growth model to the chronological ^{18}F-AV45 Aβ PET data with a single uninhibited exponential growth rate (r = 0.20 yrs[-1]) and

a single time of half maximal Aβ concentration (T_{50} = 14.9 yrs) for all brain regions in the CIC neuroanatomical atlas (Regions 1-45).
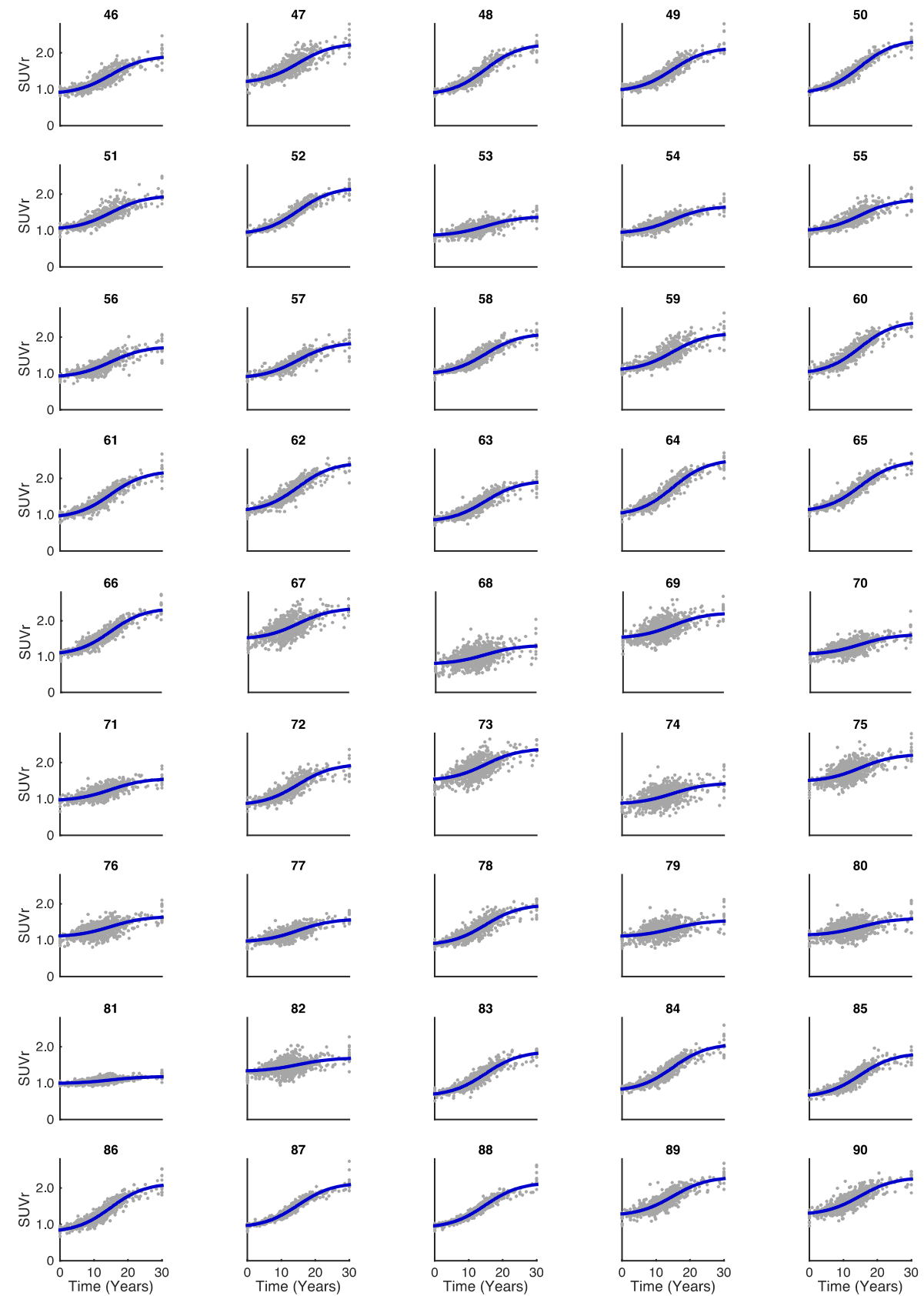
Figure S-2: Fit of the most parsimonious logistic growth model to the chronological ^{18}F-AV45 Aβ PET data with a single uninhibited exponential growth rate (r = 0.20 yrs^{-1}) and a single time of half maximal Aβ concentration (T_{50} = 14.9 yrs) for all brain regions in the CIC neuroanatomical atlas (Regions 45-90).

Parametric Imaging

Model 11 was linearized for fast and robust fitting at the voxel-level using fixed values

for r and T_{50} obtained from the regional analysis. The original model equation

$$SUVr(t) \ = \ NS + \frac{K}{1+e^{-r(t-T_{50})}}.$$

is transformed into a linear equation of the form,

$$b = A\,x$$

where

$$A = \begin{bmatrix} 1 & \frac{1}{1+e^{-r(t_1-T_{50})}} \\ \vdots & \vdots \\ 1 & \frac{1}{1+e^{-r(t_{769}-T_{50})}} \end{bmatrix} \begin{bmatrix} NS_{vox} \\ K_{vox} \end{bmatrix},$$

$$x = \begin{bmatrix} NS_{vox} \\ K_{vox} \end{bmatrix},$$

$$b = \ SUVr(t)$$

NS_{vox} and K_{vox} are the non-specific binding and the carrying capacity for the voxel

respectively. These parameters were then estimated by solving the linear equation in

MATLAB using

$$x = A\backslash b \ . \tag{11}$$

Calculation with different ROI sets

We have run the analysis process on 2 additional sets of ROIs. A set of 9 ROIs which are much larger regions and cover the whole brain along with a parcellation that is restricted to cortical region sand includes 76 regions (this corresponds to the removal of the sub-cortical regions from the previous set of 90 ROIs where there is lower accumulation).

For both these additional analyses the same model (Model 11) is identified as the most parsimonious description of the data. This provides strong evidence that this result is not dependent on the choice of regions or due to lack of statistical power in measuring changes in T_{50}.

9 Large ROIs

Model	K SUVr	r yrs^{-1}	T$_{50}$ yrs	NS	Parameters	SSQ	ΔBIC$_i$ (BIC$_i$ - BIC$_{min}$)
Model 1	Global	Global	Global	Global	4	434.4	12722.3
Model 2	Global	Local	Global	Global	12	227.7	8322.39
Model 3	Local	Global	Global	Global	12	126.9	4275.26
Model 4	Global	Global	Local	Global	12	106.2	3042.9
Model 5	Global	Global	Global	Local	12	94.15	2209.86
Model 6	Local	Local	Global	Global	20	103.5	2938.7
Model 7	Local	Global	Local	Global	20	90.9	2037.42
Model 8	Global	Local	Local	Global	20	86.13	1663.84
Model 9	Global	Global	Local	Local	20	74.93	700.218
Model 9	Global	Local	Global	Local	20	77.4	924.902
Model 11	Local	Global	Global	Local	20	67.72	0
Model 12	Local	Local	Local	Global	28	84.44	1597.98
Model 13	Local	Global	Local	Local	28	67.64	62.0933
Model 14	Global	Local	Local	Local	28	67.62	60.4626
Model 15	Local	Local	Global	Local	28	67.05	1.398
Model 16	Local	Local	Local	Local	36	67.01	68.2141

Table S-1: Analogous table to Table 2 using 9 large ROIs covering the whole cerebrum. As with the analysis using a 90 region atlas, Model 11 is selected as the optimum model.

76 Cortical ROIs

Model	K SUVr	r yrs^{-1}	T$_{50}$ yrs	NS	Parameters	SSQ	ΔBIC$_i$ (BIC$_i$ - BIC$_{min}$)
Model 1	Global	Global	Global	Global	4	1257	74781.8
Model 2	Global	Local	Global	Global	79	895.3	55777.2
Model 3	Local	Global	Global	Global	79	484.3	19862.4
Model 4	Global	Global	Local	Global	79	456.4	16390.7
Model 5	Global	Global	Global	Local	79	400.4	8738.36
Model 6	Local	Local	Global	Global	154	392	8334.23
Model 7	Local	Global	Local	Global	154	394.3	8673.35
Model 8	Global	Local	Local	Global	154	403.8	10063.6
Model 9	Global	Global	Local	Local	154	381.8	6792.16
Model 10	Global	Local	Global	Local	154	347.4	1268.12
Model 11	Local	Global	Global	Local	154	339.9	0
Model 12	Local	Local	Local	Global	229	371.3	5980.34
Model 13	Local	Global	Local	Local	229	339.6	758.079

Model 14	Global	Local	Local	Local	229	339.7	790.638
Model 15	Local	Local	Global	Local	229	336.7	272.73
Model 16	Local	Local	Local	Local	304	336.1	976.546

Table S-2: Analogous table to Table 2 using 76 cortical ROIs. Model 11 is again selected as the optimum model.